AGU100 ADVANCING EARTH AND SPACE SCIENCE

Check for updates

Tectonics

RESEARCH ARTICLE
10.1029/2019TC005590

Key Points:
- Most of the Malawi rift is along the western edge of a high seismic velocity zone possibly associated with cratonic lithosphere
- Isolated asthenospheric upwelling beneath the Malawi rift may contribute to lithospheric weakening at the early stage of continental rifting
- Low velocities under the Rungwe Volcanic Province exist in the top 200-km of the mantle, reflecting melts upwelling due to lithospheric extension

Supporting Information:
- Supporting Information S1
- Table S2
- Table S3

Correspondence to:
Y. Yu,
yuyouqiang@tongji.edu.cn

Citation:
Yu, Y., Gao, S. S., Zhao, D., & Liu, K. H. (2020). Mantle structure and flow beneath an early-stage continental rift: Constraints from ***P*** wave anisotropic tomography. *Tectonics*, *39*, e2019TC005590. https://doi.org/10.1029/2019TC005590

Received 20 MAR 2019
Accepted 18 JAN 2020
Accepted article online 22 JAN 2020

Mantle Structure and Flow Beneath an Early-Stage Continental Rift: Constraints From *P* Wave Anisotropic Tomography

Youqiang Yu[1], Stephen S. Gao[2], Dapeng Zhao[3], and Kelly H. Liu[2]

[1]State Key Laboratory of Marine Geology, Tongji University, Shanghai, China, [2]Geology and Geophysics Program, Missouri University of Science and Technology, Rolla, MO, USA, [3]Department of Geophysics, Graduate School of Science, Tohoku University, Sendai, Japan

Abstract To explore 3-D seismic velocity and radial anisotropy structures of the upper mantle and mantle transition zone beneath the Malawi and Luangwa rift zones of the East African Rift System, we conduct the first study of *P* wave anisotropic tomography using data recorded at 75 seismic stations including 34 stations that we installed along two profiles as part of the Seismic Arrays for African Rift Initiation experiment. Both rift zones are revealed to have normal or slightly low velocity anomalies in the lithosphere and upper asthenosphere. The surrounding cratonic lithosphere is characterized by high-velocity anomalies with amplitudes ranging from +1.0% to +2.0%. Negative radial anisotropy, which is indicative of upwelling or downwelling in the mantle, is mainly distributed beneath the rift zones, whereas the other areas mostly feature positive radial anisotropy that implies horizontal flow. A prominent circular low-velocity anomaly exists in the top 200 km of the upper mantle beneath the Rungwe Volcanic Province without obvious connections to the lower mantle. Combining the present findings with previous geodetic and tomography results, we interpret the Rungwe Volcanic Province magmatism as primarily due to decompression melting in response to lithospheric extension induced by the counterclockwise and clockwise rotations of the Victoria and Rovuma microplates, respectively, with respect to the Nubian plate. Isolated mantle upwelling, which is indicated by scattered low-velocity anomalies and negative radial anisotropy beneath the Malawi rift zone, may contribute to the incipient rifting.

1. Introduction

Continental rifting plays a fundamental role in the evolution of the Earth and is characterized by lateral stretching and thinning of the whole lithosphere due to active mantle upwelling or tensional intraplate far-field forces (e.g., Ruppel, 1995; Sengor & Burke, 1978). Long-lasting rifting ultimately leads to continental breakup and the birth of ocean basins (Ruppel, 1995). As a divergent boundary between the Nubian and Somalian plates (Calais et al., 2006; Saria et al., 2014; Stamps et al., 2008), the East African Rift System (EARS; Figure 1) represents a modern archetype of narrow-mode continental rifts and comprises a series of rift zones trending in a roughly north-south direction (Chorowicz, 2005). It mainly propagates along Proterozoic mobile belts and records the entire spectrum of rift development starting from the incipient phase of continental breakup in eastern Africa to nascent seafloor spreading in the Afar Depression (Bridges et al., 2012; Chorowicz, 2005; O'Donnell et al., 2013). Although extensive investigations have been conducted for the mature segments of the EARS such as the Main Ethiopian and Kenyan rifts, comparatively, few studies have been conducted for the early-stage rifting segments where the magma has not breached the surface. As the southernmost segment of the EARS, the nonvolcanic Malawi rift zone (MRZ) is an ideal locale to explore early-stage rifting mechanisms.

On the basis of the similarities between the Malawi and Tanganyika rifts in terms of the structural style, geometry, and the absence of significant volcanic activity, the MRZ is generally considered to be the southern extension of the Western Branch of the EARS (Ebinger et al., 1987). The initiation of the MRZ is almost synchronous with the onset of volcanism in the Rungwe Volcanic Province (RVP; Figure 1) in the late Miocene time (about 8.6 Ma) (Ebinger et al., 1989). The Cenozoic RVP is the only surface expression of magmatism within the southern EARS and develops within a complex accommodation zone where the Malawi rift, Rukwa rift, and Usangu basin join together (Figure 1). The MRZ is a weakly extended (<15%) continental

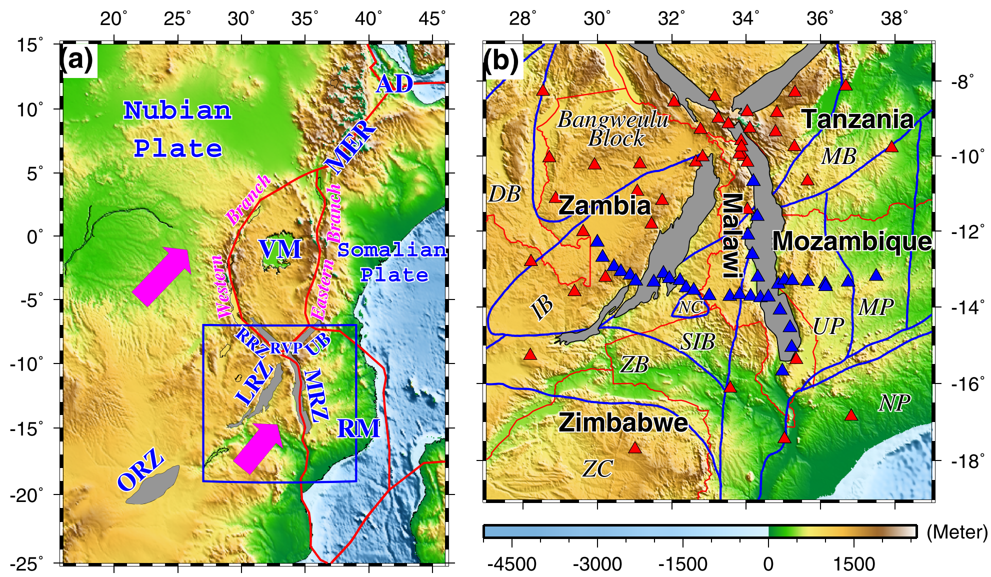

Figure 1. (a) Topography and tectonic setting of eastern Africa. The study area is highlighted by the blue rectangle. Red lines illustrate plate boundaries (Stamps et al., 2008). Pink arrows indicate the absolute motion direction of the African Plate based on the NNR-MORVEL56 model (Argus et al., 2011). Gray shaded areas indicate rift zones. (b) Tectonic base map of the Malawi and Luangwa rift zones displaying locations of the broadband seismic stations used in this study (triangles). Blue triangles indicate stations belonging to the experiment of the Seismic Arrays for African Rift Initiation (SAFARI). Red lines depict country borders, and major tectonic boundaries are plotted as blue lines (Craig et al., 2011). DB = Damara Belt; IB = Irumide Belt; MB = Mozambique Belt; MP = Marrupa Province; NC = Niassa Craton; NP = Nampula Province; SIB = Southern Irumide Belt; UP = Unango Province; ZB = Zambezi Belt; ZC = Zimbabwe Craton; AD = Afar Depression; LRZ = Luangwa rift zone; MER = Main Ethiopian rift; MRZ = Malawi rift zone; ORZ = Okavango rift zone; RM = Rovuma Microplate; RRZ = Rukwa rift zone; RVP = Rungwe Volcanic Province; UB = Usangu Basin; VM = Victoria Microplate.

rift zone that stretches over 900 km with its southern termination at the Urema graben in Mozambique (e.g., Chorowicz, 2005; Ebinger et al., 1987; Laó-Dávila et al., 2015). Compared with the MRZ, the NE-SW trending Luangwa rift zone (LRZ) better follows the orientation of preexisting orogenic belts (Craig et al., 2011) and is thought to be closely associated with the strike-slip movement in the Mwembeshi Shear Zone (Banks et al., 1995). The LRZ is located in the Mesoproterozoic-Neoproterozoic Irumide and Southern Irumide orogenic belts and situated along the margins of rigid continental blocks including the Archean-Palaeoproterozoic Bangweulu block to the northwest (Figure 1). The LRZ approximately initiated at the earliest Permian time (during the Karoo rifting) and has been reactivated by recent tectonic forces (Banks et al., 1995; Daly & Watts, 2017).

Due to the sparse coverage of seismic stations prior to the deployment of the Seismic Arrays for African Rift Initiation (SAFARI) stations (Gao et al., 2013), there was a general lack of seismological studies directly focusing on the MRZ and LRZ. Some studies of continental or global scale seismic tomography have revealed continuous low-velocity anomalies (LVAs) originating from the core-mantle boundary and extending to the crust or uppermost mantle (e.g., Adams et al., 2012; Hansen et al., 2012; Mulibo & Nyblade, 2013; Ritsema et al., 1999; Zhao, 2001), which are interpreted as representing the upwelling branch of the African superplume (Ritsema et al., 1999). Such a hypothesis has been proposed to explain the generally NE-SW trending fast orientations of shear wave splitting measurements beneath eastern Africa (Bagley & Nyblade, 2013; Tepp et al., 2018; Walker et al., 2004). However, whether the African superplume plays a key role in generating the observed seismic anisotropy and in the initiation and evolution of the EARS remains enigmatic. Based on new shear wave splitting measurements in the vicinity of the Luangwa and Malawi rifts using the SAFARI data, Reed et al. (2017) suggest that the observed azimuthal anisotropy is most likely caused by the absolute plate motion (APM) of the African Plate in the no-net-rotation (NNR) frame, with local modulation of the flow system along the edges of lithospheric roots. Recent receiver-function investigations using the SAFARI data indicate that the incipient and young segments of the EARS are generally characterized by

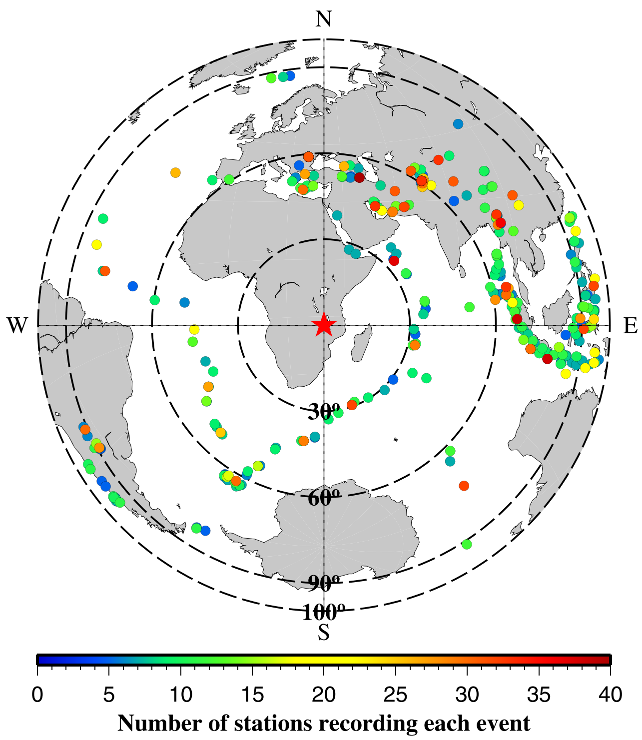

Figure 2. Epicentral distribution of the 411 teleseismic events (color dots) used in this study. Different colors indicate the number of stations that recorded each of the events. The red star shows the center of the study area.

a normal mantle transition zone (MTZ) thickness (Reed et al., 2016; Yu et al., 2015), which is inconsistent with the existence of significant thermal anomalies in the MTZ. Studies of regional-scale surface-wave and body-wave tomography (Accardo et al., 2017; Adams et al., 2012; 2018; Grijalva et al., 2018; Mulibo & Nyblade, 2013; O'Donnell et al., 2013) reveal a nearly circular LVA localized to the RVP within the uppermost mantle, which possibly represents the presence of melt (O'Donnell et al., 2016). However, whether the LVA is linked to the African superplume in the lower mantle remains debated (e.g., Grijalva et al., 2018; O'Donnell et al., 2013), mainly due to the sparse distribution of seismic stations in the vicinity of the RVP and the intrinsic limitations of the geophysical techniques.

Seismic anisotropy is believed to widely exist in the Earth's interior especially in the upper mantle. It is mostly caused by lattice-preferred or shape-preferred orientations of anisotropic minerals such as olivine in the upper mantle (Silver, 1996). Probing seismic anisotropy offers a chance to decipher both the past (fossil anisotropy preserved in the lithosphere) and current (present-day mantle flow) tectonic deformations. The shear wave splitting technique is one of the major tools frequently used to quantify azimuthal anisotropy. While it has an excellent lateral resolution, its vertical resolution is poor. More importantly, the shear wave splitting method cannot be utilized to effectively characterize anisotropy with a vertical axis of symmetry (Silver, 1996) presumably associated with mantle upwelling or downwelling. The vertical tectonic regime can be constrained by exploring radial anisotropy related to the vertical movements. Radial anisotropy is a simple type of transverse isotropy with the hexagonal symmetry assumed to be vertical and depicts the difference between the vertical and horizontal velocities. Negative radial anisotropy (i.e., vertical velocity is faster than horizontal velocity) is usually associated with the scenario of mantle upwelling or downwelling, and positive radial anisotropy may indicate horizontal mantle flow. In this study, we employ a large number of *P* wave arrival-time data from teleseismic events recorded at the SAFARI and other stations to conduct a simultaneous inversion for the 3-D distribution of isotropic *P* wave velocity (Vp) and radial anisotropy in the upper mantle and MTZ beneath the MRZ and adjacent areas.

2. Data and Methods

Data used in this study were recorded at a total of 75 broadband seismic stations of which 34 stations belong to SAFARI (Gao et al., 2013) deployed along two profiles in Malawi, Mozambique, and Zambia (Figure 1b). The other 41 stations are from seven different networks, including ZP (Africa Array- Uganda/Tanzania), AF (Africa Array), IU (Global Seismic Network), XD (Tanzania Broadband Experiment), XV (Madagascar and Comores Seismic Experiment), YH (Africa Array SE Tanzania Basin Experiment), and YI (2009 Malawi Earthquake). All the data are publicly accessible from the Incorporated Research Institutions for Seismology Data Management Center. Hypocentral parameters of the teleseismic events were downloaded from the website of the U.S. Geological Survey (http://earthquake.usgs.gov/earthquakes/search). All the events were initially selected according to the following criteria: (1) The cutoff magnitude is 4.0; (2) their epicentral distances fall in the range of 25° to 95°; and (3) they were recorded at six or more seismic stations in the present study region (Figure 1b). We manually picked the first *P* wave arrivals on the vertical-component seismograms with a high signal-to-noise ratio by referring to the theoretical arrival times calculated based on the IASP91 Earth model (Kennett & Engdahl, 1991). The picking accuracy of the arrival times is estimated to be 0.1–0.2 s (Yu et al., 2017).

The final data set used for the tomography inversions consists of 5,760 *P* wave arrivals from 411 teleseismic events (Figure 2). Relative travel time residuals are calculated for each event by subtracting the mean residual from the raw residuals so that contributions from both the hypocentral mislocations and velocity

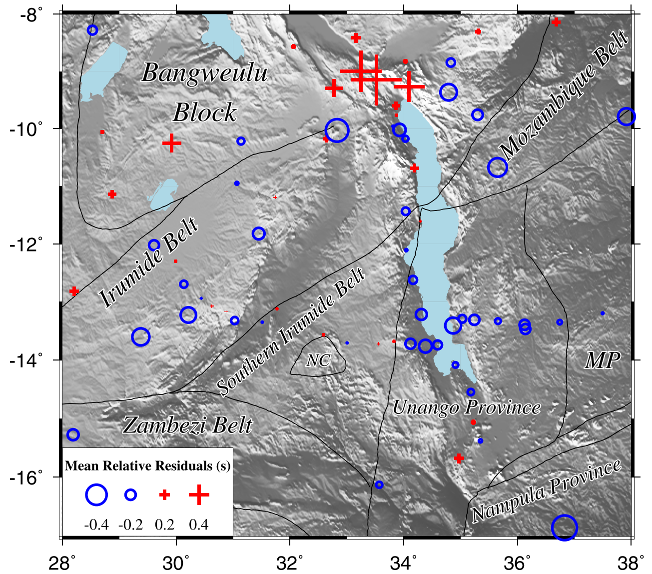

Figure 3. Map of average *P* wave relative travel time residual at each station after the crustal correction is made. Blue circles and red crosses denote early and delayed arrivals, respectively.

heterogeneities outside the study volume could be minimized (Zhao et al., 1994). In addition, the CRUST1.0 model (Laske et al., 2013) is adopted to correct for lateral variations of the crustal structure (Figure S1 in the supporting information). After the crustal correction, most of the relative travel time residuals fall in the range of −1 s to 1 s (Figure S2). The map of the average relative travel time residual at each station (Figure 3) indicates that significantly delayed arrivals (up to 1.0 s) appear at stations in the RVP. The stations located in the southern MRZ and the Irumide Belt to the west of the LRZ exhibit early arrivals. The absolute travel time residuals for each of the events have a circular average of 1.2± 0.1 s, which is comparable to that beneath southern Africa with a mean value of 1.5 ± 0.1 s (Yu et al., 2017), suggesting that a slower-than-normal mantle exists under the study region. Considering the decent azimuthal coverage of the events (Figure 2) and the lack of widespread LVAs in the upper mantle (e.g., Accardo et al., 2017; Adams et al., 2012, 2018; Fishwick, 2010; Priestley et al., 2008; Reed et al., 2017; Sebai et al., 2006), these results may reflect significant delays from the hypothesized African superplume in the lower mantle (e.g., Mulibo & Nyblade, 2013; Ritsema et al., 1999).

The IASP91 Earth model is taken to be the starting 1-D velocity model for the tomography inversions for both isotropic 3-D Vp anomalies and *P* wave radial anisotropy. The method of Zhao et al. (1994) is employed to determine a 3-D isotropic Vp model of the upper mantle by inverting the relative travel time residuals. We set up a 3-D grid with a lateral grid interval of 0.8° and a vertical grid interval of 100 km in the depth range of 100 to 600 km. Vp perturbations relative to the IASP91 Earth model at the 3-D grid nodes are taken as unknown parameters, and the Vp perturbation at any point in the study volume is calculated by linearly interpolating the Vp perturbations at the eight grid nodes surrounding that point (Zhao et al., 1992, 1994).

A model of 3-D Vp radial anisotropy in the study volume is jointly determined using the method of Wang and Zhao (2013), which was developed from the isotropic tomography method of Zhao et al. (1992, 1994). Vp radial anisotropy is assumed to have a vertical hexagonal symmetry axis. Two sets of 3-D grid are arranged in the study volume: One is a fine grid, the other is a coarse grid. The fine grid is the same as the one used to independently invert for the 3-D isotropic Vp structure. The coarse grid is adopted to invert for the Vp anisotropic parameters (Wang & Zhao, 2013), which has a lateral grid interval of 1.8° and includes three meshes at depths of 150, 300, and 450 km. The coarse grid is necessary because inverting for Vp anisotropy requires a better coverage of ray paths.

The theoretical travel time and ray path for a given pair of station and event are computed using an efficient 3-D ray tracing technique that combines the pseudo-bending algorithm and Snell's law (Zhao et al., 1992). Most of the study volume is well crisscrossed by a reasonable number of rays at each depth (Figure S3). The sparse and large system of observation equations, which relate the observed data (relative travel time residuals) to the model parameters at the 3-D grid nodes, is solved using an iterative conjugate-gradient LSQR algorithm (Paige & Saunders, 1982) with damping and smoothing regularizations (Zhao, 2001; Zhao et al., 1994). The optimal damping and smoothing parameters are determined on the basis of trade-off curves between the root-mean-square travel time residual and the norm of the 3-D Vp model (i.e., model variance). The trade-off curves are constructed by conducting a series of tomography inversions with different values of the damping and smoothing parameters (Figure S4). The optimal damping and smoothness parameters are determined to be 40.0 and 0.001, respectively (Figure S4).

3. Resolution Tests

To evaluate the robustness and spatial resolution of the resulting tomography images, we have carried out extensive synthetic tests (Figures S5–S20) with various input models. For each of the synthetic tests, a set of synthetic travel time residuals is calculated for a given input model using the same numbers of seismic stations and events as those in the real data set. Random noise (−0.2 to +0.2 s) with a standard deviation

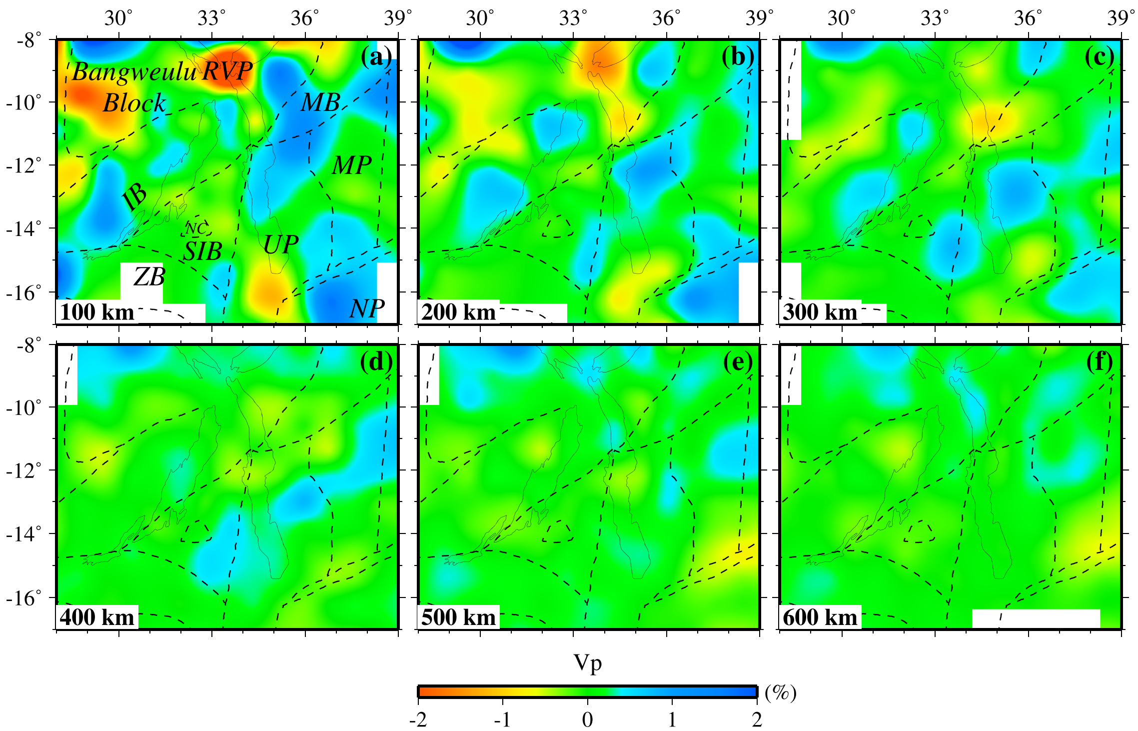

Figure 4. Map views of resulting isotropic Vp tomography at different depths as shown at the lower-left corner of each map. The red and blue colors denote low and high Vp perturbations, respectively, whose scale is shown at the bottom.

of 0.1 s is added to the synthetic data set for simulating the picking errors of the observed data. The synthetic data are then inverted to generate an output model using the same tomography method. The resolution of the resulting tomography image can be evaluated by comparing the input and output models.

We firstly performed checkerboard resolution tests (CRTs) for the isotropic Vp tomography by assigning alternating positive and negative Vp anomalies of 4% to the 3-D grid nodes. CRTs with lateral grid intervals of 0.6°, 0.8°, and 1.0° (Figures S5–S7) are conducted, and the results indicate that our isotropic Vp model has a lateral resolution of about 0.8°. To investigate the smearing effect to our tomography model, we carried out three synthetic tests with the input LVAs and HVAs existing at different depths (Figures S8–S13). The results suggest that the smearing effect is insignificant and the tomography model can be satisfactorily resolved.

Following the above procedures for examining the resolution of the isotropic Vp tomography results, we conducted similar synthetic tests to evaluate the tomography results of radial anisotropy (Figures S14–S20). In addition to isotropic Vp perturbations of ±4%, radial anisotropies with an amplitude of ±4% are alternately assigned to the 3-D nodes of the coarse grid for Vp anisotropy (Figures S14–S16). Positive and negative radial anisotropies mean that Vp in the horizontal direction is faster and slower than that in the vertical direction, respectively. We performed the CRTs with three pairs of lateral grid intervals for the radial anisotropy tomography; the lateral grid interval for the radial anisotropy is assigned to be twice of that for the isotropic Vp tomography (Figures S14–S16). In addition, we carried out CRTs with input models in which either the isotropic Vp anomalies or the anisotropic parameters are assigned as zero (Figures S17 and S18); thus, the trade-off between the isotropic Vp and radial anisotropy can be examined. The results of these extensive resolution tests show that our isotropic and anisotropic tomography images are generally robust and reliable.

4. Results

4.1. Isotropic *P* Wave Velocity Structure

Similar to the vast majority of regional body-wave tomography studies, the obtained velocity models are Vp anomalies relative to the mean Vp at each depth instead of absolute Vp values due to the use of relative travel time residuals. The resulting isotropic Vp anomalies (Table S1) clearly reflect the tectonic terranes (Figure 4) and are generally consistent with previous regional-scale tomography results (Accardo et al., 2017; Adams et al., 2012, 2018; Grijalva et al., 2018; Mulibo & Nyblade, 2013; O'Donnell et al., 2013; Pasyanos & Nyblade, 2007; Sebai et al., 2006). Most of the strong Vp anomalies exist in the upper mantle and there are no significant Vp anomalies within the MTZ, which is in agreement with the generally normal MTZ thickness under the study region revealed by a receiver-function study using a similar broadband data set (Reed et al., 2016).

The most prominent feature of the isotropic Vp model is a nearly circular LVA extending to a depth of ~200 km under the RVP, which is consistent with recent results of body-wave and surface-wave tomography focusing on the RVP and the northern terminus of the MRZ (Accardo et al., 2017; Grijalva et al., 2018). In the top 200 km, both the southern and northern sections of the MRZ show LVAs while their central part is along the western edge of a region dominated by HVAs with a NE-SW trend, which is also revealed by surface-wave tomography (Adams et al., 2018; O'Donnell et al., 2013; Pasyanos & Nyblade, 2007; Sebai et al., 2006) and suggested by the apparent shallowing of the MTZ discontinuities (Reed et al., 2016). Strong parallelism between the shallower-than-normal apparent depths of the 410- and 660-km discontinuities is observed beneath the central MRZ, suggesting that its average upper-mantle velocity is higher than normal (Reed et al., 2016). In addition, deflection of asthenospheric flow by a thick lithospheric root near the central MRZ is suggested to be responsible for sudden changes of azimuthal anisotropy inferred from shear wave splitting measurements using the SAFARI data (Reed et al., 2017). As compared to the previous results, the HVA beneath the Unango Province is much wider and extends further to the eastern flank of the MRZ, mainly due to our improved data coverage.

4.2. Depth Dependence of Radial Anisotropy

The resulting radial anisotropy (Table S2) is displayed in map views (Figure 5) and vertical cross sections (Figure 6). To test the reliability of the resulting anisotropy results and their dependence on grid size, we performed tomography inversions with a larger grid interval of 2.0°. The results (Figures 5d–5f) are generally consistent with those obtained with a grid interval of 1.8° (Figures 5a–5c) except for some changes at 150-km depth around the RVP and its nearby areas. In the lithospheric upper mantle (150-km depth in Figures 5a and 5d), positive radial anisotropy (i.e., horizontal Vp > vertical Vp) is revealed beneath the Bangweulu Block, the RVP, and the southern tip of the MRZ. Negative radial anisotropy in the lithosphere is mostly found beneath areas where high-velocity lithospheric roots are imaged such as the Irumide Belt, the Nampula Province and the northeastern Malawi rift. A similar feature is also revealed in some cratonic regions where negative radial anisotropy occurs, such as the East European platform and the Arabian shield (Chang et al., 2010).

In the asthenospheric upper mantle (Figures 5b and 5e) and MTZ (Figures 5c and 5f), prominent negative radial anisotropy is revealed beneath the northern part of the study area. In comparison, both the RVP and MRZ are generally characterized by weak negative radial anisotropies. However, a distinguished regional feature is revealed beneath the MRZ where strong negative radial anisotropy exists in the MTZ. Most of the tectonic regions outside the rift zones of the EARS generally exhibit positive radial anisotropy below the lithosphere.

5. Discussion

5.1. Lateral Heterogeneity in the Lithosphere

The area dominated by HVAs (Figure 4) traversing the MRZ is spatially consistent with the region with a thick (180–200 km) lithosphere across the southern MRZ revealed by seismic tomography (Fishwick, 2010), the apparent shallowing of the MTZ discontinuities (Reed et al., 2016), and gravity modeling (Njinju et al., 2019). Previous tomography results of the African continent indicate that the lithosphere beneath the LRZ and MRZ seems to be connected with the Congo and Kalahari cratons in a larger scale (Fishwick, 2010; Priestley et al., 2008; Sebai et al., 2006). A recent study of Rayleigh-wave tomography proposes that the Bangweulu Block, the Irumide Belt and the central Malawi rift are an assemblage of Archean cratonic roots based on the observed high velocities at longer periods (Adams et al., 2018). Thus, we speculate that the robust HVAs revealed in the upper mantle possibly represent the eastward extension of the cratonic lithosphere spanning the Congo and Kalahari cratons (Reed et al., 2017). Most parts of the MRZ and LRZ are mostly situated along the edges of these cratonic blocks (Figures 4a and

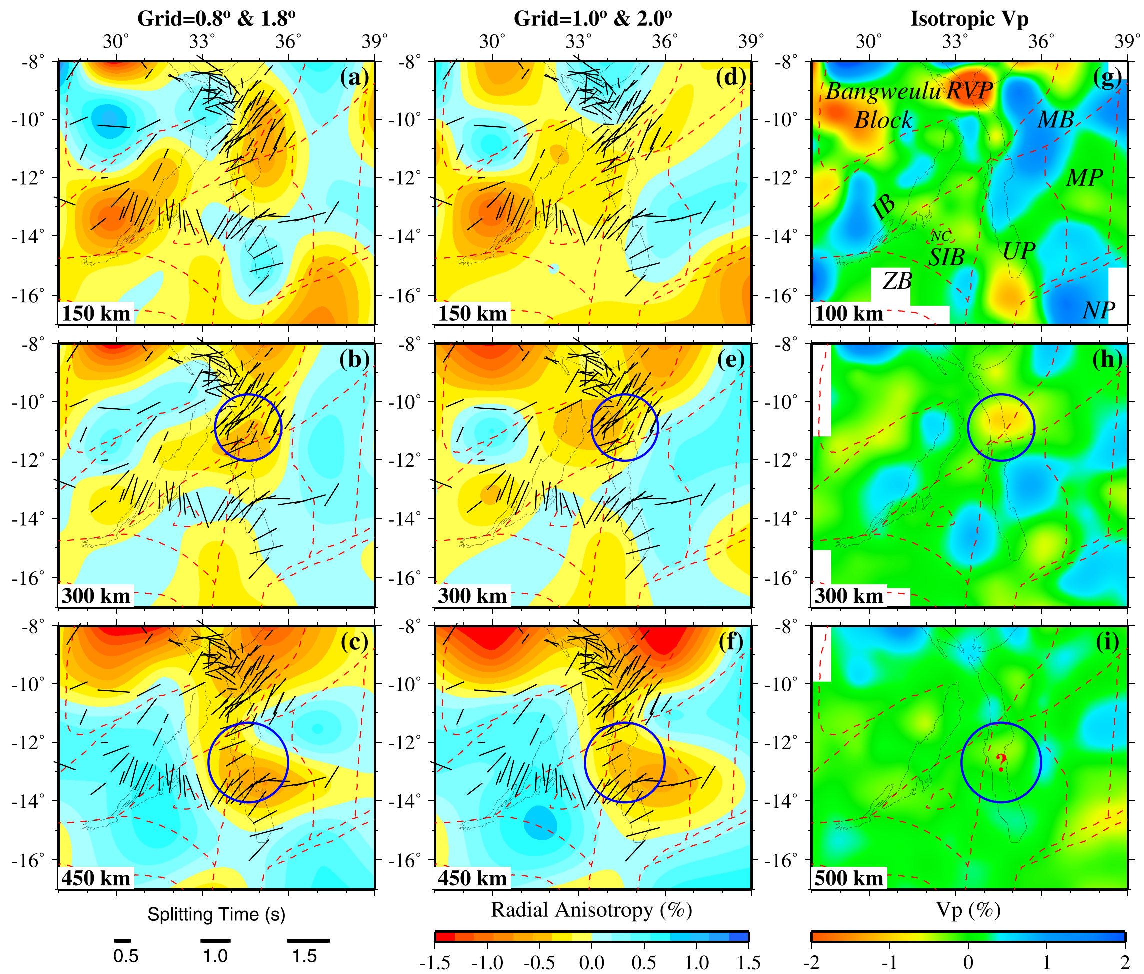

Figure 5. Map views of *P* wave radial anisotropy tomography. (a–c) Results obtained with lateral grid intervals of 0.8° and 1.8° for inverting for the isotropic Vp and radial anisotropy, respectively. (d–f) Results obtained with lateral grid intervals of 1.0° and 2.0° for inverting the isotropic Vp and radial anisotropy, respectively. The colors show the strength of radial anisotropy, whose scale is shown at the bottom right. Blue and red colors denote faster velocity in the horizontal and vertical directions, respectively. The black bars represent fast orientations of shear wave splitting measurements (Bagley & Nyblade, 2013; Reed et al., 2017; Tepp et al., 2018; Walker et al., 2004). (g–i) The resulting isotropic Vp tomography at depths of 100, 300, and 500 km from Figure 4. Blue circles indicate the locations of a possible mantle upwelling.

4b) possibly due to localized strain of preexisting fabrics (Kolawole et al., 2018; Laó-Dávila et al., 2015), a conclusion that is consistent with the apparent depths of the mantle transition zone depths (Reed et al., 2016) and shear wave splitting measurements (Reed et al., 2017) obtained using the SAFARI data set.

5.2. Isolated Mantle Upwelling and Incipient Rifting

Our radial anisotropy results (Figures 5 and 6) provide constraints on the mantle flow dynamics. Azimuthal anisotropy is sensitive to horizontal flow that can be well constrained by shear wave splitting measurements (Bagley & Nyblade, 2013; Reed et al., 2017; Tepp et al., 2018; Walker et al., 2004), while radial anisotropy helps distinguish whether the mantle flow is dominantly vertical or horizontal. The dominantly NE-SW fast orientations from shear wave splitting measurements (Bagley & Nyblade, 2013; Reed et al., 2017; Tepp et al., 2018; Walker et al., 2004) are inconsistent with the strike of most of the major lithospheric fabrics, suggesting a mostly asthenospheric origin of the observed azimuthal anisotropy. This hypothesis is consistent with results from spatial coherency analysis of shear wave splitting parameters (Gao & Liu, 2012; Reed et al., 2017), which place the origin of the inferred azimuthal anisotropy approximately at the lithosphere-asthenosphere boundary. In addition, the majority of the observed fast orientations in the study area are

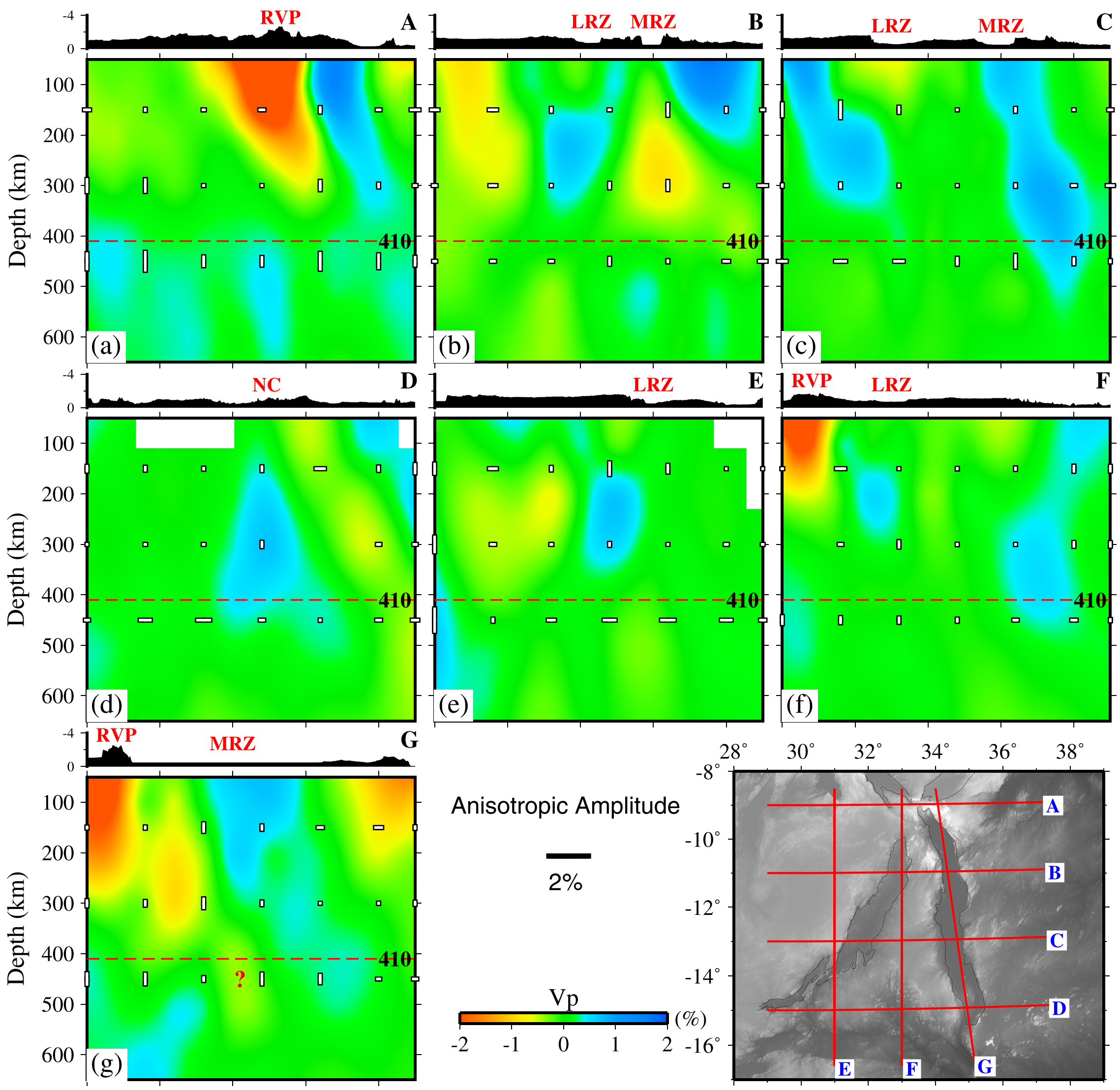

Figure 6. Vertical cross sections of isotropic Vp tomography (colors) and radial anisotropy (white bars) along the seven profiles shown on the inset map. The vertical and horizontal white bars denote faster velocity in the vertical and horizontal directions, respectively. The bar length indicates the amplitude of radial anisotropy. The dashed line in each panel denotes the 410-km discontinuity.

subparallel to the predicted NE APM direction of the African plate under the NNR model (Argus et al., 2011) and are proposed to be primarily related to APM-related simple shear within a rheologically transitional layer between the lithosphere and asthenosphere (Reed et al., 2017; Tepp et al., 2018).

Analysis on the stresses acting on the African plate based on a global finite element model of the lithosphere indicates that the current total stress is not enough to break up the thick and cold continental lithosphere (Kendall & Lithgow-Bertelloni, 2016). A factor considered necessary for rift initiation is the presence of melt caused by magma injection, which can greatly reduce the strength of the cratonic lithosphere and facilitate rifting (Bastow et al., 2010; Buck, 2004; Kendall & Lithgow-Bertelloni, 2016). Recent *P* and *S* wave tomography models developed for the northern MRZ and the RVP indicate that the lithosphere beneath the MRZ may have been weakened prior to rifting (Grijalva et al., 2018). Anomalies with significant negative radial anisotropy are revealed in the asthenosphere and MTZ under the MRZ, which are coincidently characterized as weak LVAs (Figure 5) or thin MTZ thickness (Reed et al., 2016). Such a consistence possibly indicates the existence of isolated mantle upwelling through some vertical and narrow (equal to or less than 100 km) pipes. The isolated mantle upwelling may originate from a mantle plume. However, investigations of lithospheric stresses focusing on the EARS suggest that buoyancy forces arising from gravitational potential energy gradients within the lithosphere are sufficient to drive the Nubia-Somalia divergence. Additional contributions from diverging mantle flow associated with the African Superplume would overestimate surface kinematics (Stamps et al., 2014). Thus, lithospheric stretching related to the plate motions may primarily drive the incipient rifting of the MRZ considering the dominant APM-parallel NE-SW fast orientations (Reed et al., 2017; Tepp et al., 2018) and the absence of widespread MTZ thinning (Reed et al., 2016). The isolated mantle upwelling as revealed by the sublithospheric negative radial anisotropy beneath the MRZ may help initiate continental breakup in regions of unaltered lithosphere (Buck, 2004; Stamps et al., 2014). The isolated regions with negative radial anisotropy and HVAs might represent downwelling of cold material associated with mantle upwelling beneath the MRZ (e.g., Yu & Zhao, 2018).

5.3. Decompression Melting Beneath the Rungwe Volcanic Province

The existence of a pronounced LVA within the lithospheric mantle and uppermost asthenosphere beneath the Cenozoic RVP (Figures 4 and 6a) suggests the localization of magmatism possibly controlled by upper mantle processes. Localized weakening of the lithosphere associated with extension and elevated temperatures (Carlson & Gangi, 1985; Ruppel, 1995) is a common mechanism to explain velocity reductions beneath rift zones (Accardo et al., 2017). Recent *P* and *S* wave tomography studies regard the LVA beneath the RVP as the consequence of the flow of warm, superplume mantle from the southwest, upwelling beneath, and around the Bangweulu Craton lithosphere (Grijalva et al., 2018). This suggestion is inconsistent with our observations. Our results show that the LVA beneath the RVP is mostly constrained to the upper mantle above 200-km depth and has no observable connection with the underlying deeper mantle. Thus, volcanism is unlikely associated with an active mantle plume existing directly beneath the RVP. Instead, decompression melting related to lithospheric extension is possibly the dominant mechanism leading to the development of volcanic activities beneath the RVP, which is revealed to experience the greatest lithospheric thinning based on results of surface wave tomography (Accardo et al., 2017).

The RVP acts as the nexus of three rigid blocks, including the Nubian plate, the Victoria and the Rovuma microplates (Calais et al., 2006). The Rovuma microplate is separating from the Nubian Plate with a maximum eastward spreading rate of 2.2 mm/year at the northern tip of the MRZ (Saria et al., 2014). Geodetic evidence (Calais et al., 2006) indicates that the Rovuma and Victoria microplates are rotating clockwise and counterclockwise with respect to the Nubia Plate, respectively, offering a driving force for the occurrence of extensional deformation and lithospheric thinning beneath the RVP. Once the lithosphere beneath the RVP is weakened and thinned, decompression melting is expected to occur, leading to the observed low velocities and surface volcanism. Such a dynamic process is supported by not only the observed localized LVA in the shallow upper mantle but also the resulting radial anisotropy beneath the RVP. Positive (dominantly horizontal) and negative (dominantly vertical) radial anisotropies are observed in the lithosphere and asthenosphere beneath the RVP, respectively (Figures 5 and 6). The presence of melt has been consistently supported by various previous tomography studies (Accardo et al., 2017; Grijalva et al., 2018; O'Donnell et al., 2016). The alignment of melt pockets or magma-filled cracks tends to produce rift-parallel azimuthal anisotropy (Tepp et al., 2018), leading to significant radial anisotropy dominantly in the horizontal direction. Thus, the positive radial anisotropy in the lithosphere beneath the RVP can be attributed to the lattice-preferred orientation of seismically anisotropic minerals in response to the finite strains accompanying extension and is widely observed in the western United States (Huang & Zhao, 2013; Moschetti et al., 2010; Yu & Zhao, 2018).

6. Conclusions

In this study, we jointly determine the first high-resolution images of *P* wave velocity and radial anisotropy tomography beneath the Malawi and Luangwa rift zones by inverting a large number of teleseismic *P* wave travel time data. The absence of widespread LVAs within the MTZ is inconsistent with a dominant role played by the hypothesized African superplume on rifting and volcanism in the study area. The HVA with a NE-SW trend east of the MRZ possibly represents thick cratonic lithosphere. Negative radial anisotropy is revealed beneath the MRZ and possibly indicates small-scale mantle upwelling, which may contribute to lithospheric weakening at the early stage of continental rifting. A circular-shaped prominent LVA is confined to the shallow upper mantle beneath the RVP and exhibits negative and positive radial anisotropies in the asthenosphere and lithosphere, respectively, which can be explained by upwelling and horizontal spreading of melts.

Acknowledgments

All the data used in this study are publicly available from the Incorporated Research Institutions for Seismology Data Management Center (https://ds.iris.edu/ds/nodes/dmc/). We appreciate Cory Reed, Shane Ingate, Patrick R. N. Chindandali, Belarmino Massingue, Hassan Mdala, Daniel Mutamina, Gift Navilembo, Joseph Kayenta, and Francis Tchilongola for their field assistance of seismic data acquisition in Malawi, Mozambique, and Zambia. Thoughtful reviews from F. Illsley-Kemp and J. P. O'Donnell significantly improved this manuscript. This study was supported by research grants from the National Program on Global Changing and Air-Sea Interaction (grant GASI-GEOGE-05), the National Natural Science Foundation of China (grant 41606043), the United States National Science Foundation (grants EAR-1009946 and EAR-1460516), the Japan Society for the Promotion of Science (JSPS grant 19H01996), and the Core Research Cluster of Disaster Science in Tohoku University (a Designated National University in Japan).

References

Accardo, N. J., Gaherty, J. B., Shillington, D. J., Ebinger, C. J., Nyblade, A. A., Mbogoni, G. J., et al. (2017). Surface wave imaging of the weakly extended Malawi Rift from ambient-noise and teleseismic Rayleigh waves from onshore and lake-bottom seismometers. *Geophysical Journal International*, *209*(3), 1892–1905. https://doi.org/10.1093/gji/ggx133

Adams, A., Miller, J., & Accardo, N. (2018). Relationships between lithospheric structures and rifting in the East African Rift System: A Rayleigh wave tomography study. *Geochemistry, Geophysics, Geosystems*, *19*, 3793–3810. https://doi.org/10.1029/2018GC007750

Adams, A., Nyblade, A., & Weeraratne, D. (2012). Upper mantle shear wave velocity structure beneath the East African plateau: Evidence for a deep, plateau-wide low velocity anomaly. *Geophysical Journal International*, *189*(1), 123–142. https://doi.org/10.1111/j.1365-246X.2012.05373.x

Argus, D. F., Gordon, R. G., & DeMets, C. (2011). Geologically current motion of 56 plates relative to the no-net-rotation reference frame. *Geochemistry, Geophysics, Geosystems*, *12*, Q11001. https://doi.org/10.1029/2011GC003751

Bagley, B., & Nyblade, A. A. (2013). Seismic anisotropy in eastern Africa, mantle flow, and the African superplume. *Geophysical Research Letters*, *40*, 1500–1505. https://doi.org/10.1002/grl.50315

Banks, N. L., Bardwell, K. A., & Musiwa, S. (1995). Karoo Rift basins of the Luangwa Valley, Zambia. *Geological Society of London, Special Publication*, *80*, 285–295. https://doi.org/10.1144/GSL.SP.1995.080.01.13

Bastow, I. D., Pilidou, S., Kendall, J.-M., & Stuart, G. W. (2010). Melt-induced seismic anisotropy and magma assisted rifting in Ethiopia: Evidence from surface waves. *Geochemistry, Geophysics, Geosystems*, *11*, Q0AB05. https://doi.org/10.1029/2010GC003036

Bridges, D. L., Mickus, K., Gao, S. S., Abdelsalam, M. G., & Alemu, A. (2012). Magnetic stripes of a transitional continental rift in Afar. *Geology*, *40*(3), 203–206. https://doi.org/10.1130/G32697.1

Buck, W. R. (2004). Consequences of asthenospheric variability on continental rifting. In G. D. Karner, B. Taylor, N. W. Driscoll, & D. L. Kohlstedt (Eds.), *Rheology and Deformation of the Lithosphere at Continental Margins* (pp. 1–30). New York: Columbia University Press.

Calais, E., Ebinger, C. J., Hartnady, C., & Nocquet, J.-M. (2006). Kinematics of the East African Rift from GPS and earthquake slip vector data. *Geological Society of London, Special Publication*, *259*, 9–22. https://doi.org/10.1144/GSL.SP.2006.259.01.03

Carlson, R. I., & Gangi, A. I. (1985). Effect of cracks on the pressure dependence of *P*-wave velocities in crystalline rocks. *Journal of Geophysical Research*, *90*, 8675–8684. https://doi.org/10.1029/JB090iB10p08675

Chang, S. J., Van Der Lee, S., Matzel, E., & Bedle, H. (2010). Radial anisotropy along the Tethyan margin. *Geophysical Journal International*, *182*(2), 1013–1024. https://doi.org/10.1111/j.1365-246X.2010.04662.x

Chorowicz, J. (2005). The East African rift system. *Journal of African Earth Sciences*, *43*, 379–410. https://doi.org/10.1016/j.jafrearsci.2005.07.019

Craig, T. J., Jackson, J. A., Priestley, K., & McKenzie, D. (2011). Earthquake distribution patterns in Africa: Their relationship to variations in lithospheric and geological structure, and their rheological implications. *Geophysical Journal International*, *185*, 403–434. https://doi.org/10.1111/j.1365-246X.2011.04950.x

Daly, M. C., & Watts, A. B. (2017). Neogene rift propagation of the East African Rift System (EARS) into Central Africa and its implications: Tectonic, topographic and geomorphic impacts of the Luangwa and Luapula Rift Valleys on the Upper Congo Drainage Basin, Lake Bangweulu Wetlands and the development of the diffuse southwestern tip of the EARS. In AGU Fall Meeting Abstracts.

Ebinger, C. J., Deino, A. L., Drake, R. E., & Tesha, A. L. (1989). Chronology of volcanism and rift basin propagation: Rungwe volcanic province, East Africa. *Journal of Geophysical Research*, *94*(B11), 15785–15803. https://doi.org/10.1029/JB094iB11p15785

Ebinger, C. J., Rosendahl, B. R., & Reynolds, D. J. (1987). Tectonic model of the Malawi rift, Africa. *Tectonophysics*, *141*(1-3), 215–235. https://doi.org/10.1016/0040-1951(87)90187-9

Fishwick, S. (2010). Surface wave tomography: Imaging of the lithosphere-asthenosphere boundary beneath central and southern Africa. *Lithos*, *120*, 63–73. https://doi.org/10.1016/j.lithos.2010.05.011

Gao, S. S., & Liu, K. H. (2012). AnisDep: A FORTRAN program for the estimation of the depth of anisotropy using spatial coherency of shear-wave splitting parameters. *Computational Geosciences*, *49*, 330–333. https://doi.org/10.1016/j.cageo.2012.01.020

Gao, S. S., Liu, K. H., Reed, C. A., Yu, Y., Massinque, B., Mdala, H., et al. (2013). Seismic arrays to study African rift initiation. *Eos, Transactions American Geophysical Union*, *94*, 213. https://doi.org/10.1002/2013EO240002

Grijalva, A., Nyblade, A. A., Homman, K., Accardo, N. J., Gaherty, J. B., Ebinger, C. J., et al. (2018). Seismic evidence for plume- and craton-influenced upper mantle structure beneath the northern Malawi rift and the Rungwe Volcanic Province, East Africa. *Geochemistry, Geophysics, Geosystems*, *19*(10), 3980–3994. https://doi.org/10.1029/2018GC007730

Hansen, S. E., Nyblade, A. A., & Benoit, M. H. (2012). Mantle structure beneath Africa and Arabia from adaptively parameterized *P*-wave tomography: Implications for the origin of Cenozoic Afro-Arabian tectonism. *Earth and Planetary Science Letters*, *319–320*, 23–34. https://doi.org/10.1016/j.epsl.2011.12.023

Huang, Z., & Zhao, D. (2013). Mapping *P*-wave azimuthal anisotropy in the crust and upper mantle beneath the United States. *Physics of the Earth and Planetary Interiors*, *225*, 28–40.

Kendall, J. M., & Lithgow-Bertelloni, C. (2016). Why is Africa rifting? *Geological Society - Special Publications*, *420*, SP420–SP417. https://doi.org/10.1144/SP420.17

Kennett, B., & Engdahl, E. R. (1991). Traveltimes for global earthquake location and phase identification. *Geophysical Journal International*, *105*(2), 429–465. https://doi.org/10.1111/j.1365-246X.1991.tb06724.x

Kolawole, F., Atekwana, E. A., Laó-Dávila, D. A., Abdelsalam, M. G., Chindandali, P. R., Salima, J., & Kalindekafe, L. (2018). Active deformation of Malawi Rift's North Basin hinge zone modulated by reactivation of preexisting Precambrian shear zone fabric. *Tectonics*, *37*, 683–704. https://doi.org/10.1002/2017TC004628

Laó-Dávila, D. A., Al-Salmi, H. S., Abdelsalam, M. G., & Atekwana, E. A. (2015). Hierarchical segmentation of the Malawi Rift: The influence of inherited lithospheric heterogeneity and kinematics in the evolution of continental rifts. *Tectonics*, *34*, 2399–2417. https://doi.org/10.1002/2015TC003953

Laske, G., Masters, G., Ma, Z. T., & Pasyanos, M. (2013). Update on CRUST1.0—A 1-degree global model of Earth's crust. Geophys. Res. Abstracts, 15, Abstract EGU2013-2658.

Moschetti, M. P., Ritzwoller, M. H., Lin, F., & Yang, Y. (2010). Seismic evidence for widespread western-US deep-crustal deformation caused by extension. *Nature*, *464*(7290), 885–889. https://doi.org/10.1038/nature08951

Mulibo, G. D., & Nyblade, A. A. (2013). The *P* and *S* wave velocity structure of the mantle beneath eastern Africa and the African superplume anomaly. *Geochemistry, Geophysics, Geosystems*, *14*, 2696–2715. https://doi.org/10.1002/ggge.20150

Njinju, E. A., Atekwana, E. A., Stamps, D. S., Abdelsalam, M. G., Atekwana, E. A., Mickus, K. L., et al. (2019). Lithospheric structure of the Malawi Rift: Implications for magma-poor rifting processes. *Tectonics*, *38*(11), 3835–3853. https://doi.org/10.1029/2019TC005549

O'Donnell, J. P., Adams, A., Nyblade, A. A., Mulibo, G. D., & Tugume, F. (2013). The uppermost mantle shear wave velocity structure of eastern Africa from Rayleigh wave tomography: Constraints on rift evolution. *Geophysical Journal International*, *194*(2), 961–978. https://doi.org/10.1093/gji/ggt135

O'Donnell, J. P., Selway, K., Nyblade, A. A., Brazier, R. A., Tahir, N. E., & Durrheim, R. J. (2016). Thick lithosphere, deep crustal earthquakes and no melt: A triple challenge to understanding extension in the western branch of the east African rift. *Geophysical Journal International*, *204*, 985–998. https://doi.org/10.1093/gji/ggv492

Paige, C. C., & Saunders, M. A. (1982). LSQR—An algorithm for sparse linear equations and sparse least-squares. *ACM Trans. Math. Software*, *8*, 43–71. https://doi.org/10.1145/355984.355989

Pasyanos, M. E., & Nyblade, A. A. (2007). A top to bottom lithospheric study of Africa and Arabia. *Tectonophysics*, *444*(1-4), 27–44. https://doi.org/10.1016/j.tecto.2007.07.008

Priestley, K., McKenzie, D., Debayle, E., & Pilidou, S. (2008). The African upper mantle and its relationship to tectonics and surface geology. *Geophysical Journal International*, *175*(3), 1108–1126. https://doi.org/10.1111/j.1365-246X.2008.03951.x

Reed, C. A., Liu, K. H., Chindandali, P. R. N., Massingue, B., Mdala, H., Mutamina, D., et al. (2016). Passive rifting of thick lithosphere in the southern East African Rift: Evidence from mantle transition zone discontinuity topography. *Journal of Geophysical Research - Solid Earth*, *121*, 8068–8079. https://doi.org/10.1002/2016JB013131

Reed, C. A., Liu, K. H., Yu, Y., & Gao, S. S. (2017). Seismic anisotropy and mantle dynamics beneath the Malawi Rift Zone, East Africa. *Tectonics*, *36*, 1338–1351. https://doi.org/10.1002/2017TC004519

Ritsema, J., van Heijst, H. J., & Woodhouse, J. H. (1999). Complex shear wave velocity structure imaged beneath Africa and Iceland. *Science*, *286*(286), 1925–1928. https://doi.org/10.1126/science.286.5446.1925

Ruppel, C. (1995). Extensional processes in continental lithosphere. *Journal of Geophysical Research*, *100*(B12), 24187–24215. https://doi.org/10.1029/95JB02955

Saria, E., Calais, E., Stamps, D. S., Delvaux, D., & Hartnady, C. J. H. (2014). Present-day kinematics of the East African Rift. *Journal of Geophysical Research - Solid Earth*, *119*(4), 3584–3600. https://doi.org/10.1002/2013JB010901

Sebai, A., Stutzmann, E., Montagner, J. P., Sicilia, D., & Beucler, E. (2006). Anisotropic structure of the African upper mantle from Rayleigh and Love wave tomography. *Physics of the Earth and Planetary Interiors*, *155*(1-2), 48–62. https://doi.org/10.1016/j.pepi.2005.09.009

Sengor, A. M., & Burke, K. (1978). Relative timing of rifting and volcanism on Earth and its tectonic implications. *Geophysical Research Letters*, *5*, 419–421. https://doi.org/10.1029/GL005i006p00419

Silver, P. G. (1996). Seismic anisotropy beneath the continents: Probing the depths of geology. *Annual Review of Earth and Planetary Sciences*, *24*, 385–432. https://doi.org/10.1146/annurev.earth.24.1.385

Stamps, D. S., Calais, E., Saria, E., Hartnady, C., Nocquet, J., Ebinger, C. J., & Fernandes, R. M. (2008). A kinematic model for the east African rift. *Geophysical Research Letters*, *35*, L05304. https://doi.org/10.1029/2007GL03278

Stamps, D. S., Flesch, L. M., Calais, E., & Ghosh, A. (2014). Current kinematics and dynamics of Africa and the East African Rift System. *Journal of Geophysical Research - Solid Earth*, *119*, 5161–5186. https://doi.org/10.1002/2013JB010717

Tepp, G., Ebinger, C. J., Zal, H., Gallacher, R., Accardo, N., Shillington, D. J., et al. (2018). Seismic anisotropy of the upper mantle below the Western rift, East Africa. *Journal of Geophysical Research*, *123*(7), 5644–5660. https://doi.org/10.1029/2017JB015409

Walker, K. T., Nyblade, A. A., Klemperer, S. L., Bokelmann, G. H. R., & Owens, T. J. (2004). On the relationship between extension and anisotropy: Constraints from shear wave splitting across the east African plateau. *Journal of Geophysical Research*, *109*, B08302. https://doi.org/10.1029/2003JB002866

Wang, J., & Zhao, D. (2013). *P*-wave tomography for 3-D radial and azimuthal anisotropy of Tohoku and Kyushu subduction zones. *Geophysical Journal International*, *193*, 1166–1181. https://doi.org/10.1093/gji/ggt086

Yu, Y., Liu, K. H., Huang, Z., Zhao, D., Reed, C. A., Moidaki, M., et al. (2017). Mantle structure beneath the incipient Okavango rift zone in southern Africa. *Geosphere*, *13*(1), 102–111. https://doi.org/10.1130/GES01331.1

Yu, Y., Liu, K. H., Moidaki, M., Reed, A. C., & Gao, S. S. (2015). No thermal anomalies in the mantle transition zone beneath an incipient continental rift: Evidence from the first receiver function study across the Okavango rift zone, Botswana. *Geophysical Journal International*, *202*, 1407–1418. https://doi.org/10.1093/gji/ggv229

Yu, Y., & Zhao, D. (2018). Lithospheric deformation and asthenospheric flow associated with the Isabella anomaly in Southern California. *Journal of Geophysical Research - Solid Earth*, *123*, 8842–8857. https://doi.org/10.1029/2018JB015873

Zhao, D. (2001). Seismic structure and origin of hotspots and mantle plumes. *Earth and Planetary Science Letters*, *192*, 251–265.

Zhao, D., Hasegawa, A., & Horiuchi, S. (1992). Tomographic imaging of *P* and *S* wave velocity structure beneath northeastern Japan. *Journal of Geophysical Research*, *97*, 19,909–19,928. https://doi.org/10.1029/92JB00603

Zhao, D., Hasegawa, A., & Kanamori, H. (1994). Deep structure of Japan subduction zone as derived from local, regional, and teleseismic events. *Journal of Geophysical Research*, *99*, 22,313–22,329. https://doi.org/10.1029/94JB01149